Shape-programmable fluid bubbles for responsive building skins

Authors: Raphael Kay[1,2,3]*, Kevin Nitièma[2], Charlie Katrycz[3], J. Alstan Jakubiec[2,4], Nicholas Hoban[2], Benjamin D. Hatton[3]

Affiliations

[1]Department of Mechanical and Industrial Engineering, University of Toronto; 5 King's College Road, Toronto, Ontario, M5S 3G8.

[2]John H. Daniels Faculty of Architecture, Landscape and Design, University of Toronto; 1 Spadina Crescent, Toronto, Ontario, M5S 2J5.

[3]Department of Materials Science and Engineering, University of Toronto; 184 College St, Toronto, Ontario, M5S 3E4.

[4]School of the Environment, University of Toronto; 149 College Street, Toronto, Ontario, M5T 1P5.

*Corresponding author. Email: raphael.kay@mail.utoronto.ca

Abstract

Building facades that can dynamically absorb light in the visible and near-infrared region of the electromagnetic spectrum enable temporally-programmable optical control and improved building energy-efficiency. Conventional solid-phase chromogenic materials suffer performance limitations that might be addressed by highly-mobile, self-assembling, gas- and liquid-phase alternatives. Here, we introduce a fluidic interface for buildings that can achieve light modulation through reversible injections of air bubbles with self-organizing morphologies. We establish criteria for injection-rate- and flow-field-dependent bubble shape. And we demonstrate experimental control over visible light transmission, near-infrared light transmission, solar heat gain, and indoor temperature, through active modulation of bubble size. Energy models help predict the comparative operational performance of our system, allowing us to couple motion-sensing capabilities with digitally-actuated bubble formation, towards demonstrating the potential for a tunable fluidic mechanism in responsive building design.

Keywords: *self-assembly, active optics, fluidics, dynamic architecture*

1. Introduction

Buildings typically interface with the environment statically.[1] Their outer facades, which regulate the ingress and egress of energy between interior and exterior regimes, are conventionally designed as hybrid systems of fixed thermal insulators (e.g., walls) and fixed optical conductors (e.g., windows).[2] This static disposition critically undermines energy performance; buildings aim to maintain a constant indoor environment, but cannot tune material properties to quickly address hourly, diurnal, and seasonal fluctuations in exterior temperature, daylight availability, and radiative solar intensity.[3, 4] The development of active building facades, capable of achieving on-demand responses to these solar fluctuations, has emerged as an important scientific and engineering challenge.[5]

Conventional mechanisms to control light transmission through the building facade are generally either low-resolution, impractical, or expensive. Most conventionally, buildings actively shade through manual or automated blinds, controlled on the interior side of the facade.[6] Related mechanical proof-of-concept systems have also been reported, including rotating fritting structures,[7] bending elements,[8] and active microscopic and milliscopic daylight-regulating louvers,[9, 10] each able to modulate shading density. Unfortunately, some of these mechanical systems are low-resolution, rigid, and prone to failure, and have only been implemented within a handful of buildings to date.[1] Stimulus-responsive mechanisms have also been proposed for dynamic shading applications, where local environmental changes, rather than mechanical actuations, drive material configuration. For instance, moisture uptake in hygroscopic materials, driven by vapor pressure gradients, can cause a macroscopic change in material structure.[11-13] Similar efforts have been established to develop thermo- and photochromics, which modulate optical transmission in response to light intensity and temperature.[14-16] Despite the potential to achieve local actuation without a supplied energy source, the inability to decouple these material responses from their dedicated environmental stimuli limits applicability within real-life building environments.[15] Electrochromic devices have also been developed for buildings, where a controllable electric potential can be leveraged to modulate optical transparency.[15, 17, 18] While the functional performance of these systems has improved drastically over the years, their manufacturing remains costly and complex.[3, 18]

In this paper, we introduce an entirely new chromogenic platform, leveraging the pressure-induced emergence of air bubbles to control optical transmission within a confined multifluidic building layer. Based on well-established fluid-dynamic instabilities, we demonstrate systematic digital control over bubble morphology and bubble size. And we show that dynamic air bubble injections can be used to modulate visible light transmission, near-infrared light transmission, and radiative heat flow to regulate solar ingress in the built environment.

2. Bubble Self-assembly Background

When a fluid of lower viscosity is forced with pressure into a second fluid of higher viscosity, the interface between fluids becomes unstable.[19] While first observed in oil fields, where the interface between water and oil is susceptible to bifurcation and branching during oil extraction, this nonlinear fluidic phenomenon has fascinated physicists and mathematicians for nearly a century.[19, 20] Known as viscous fingering, this instability is most commonly studied within quasi-two-dimensional venues, known as Hele-Shaw cells, where one fluid is introduced into the next between two closely-spaced rigid plates.[21-24]

As first demonstrated by Saffman and Taylor,[19] the interface between the injected ‘guest’ fluid (e.g., air) and displaced 'host' fluid within a Hele-Shaw cell will become unstable, and is suspectable to fractal-like branching, if the amplification factor of a branch width, $a_\lambda > 0$, for

$$(1) \qquad a_\lambda = 3V\Delta n - \sigma\left(\frac{\pi b}{\lambda}\right)^2$$

Here, flow in the vertical plane due to buoyant forces is assumed to be negligible, V is the velocity of the fluid bubble (e.g., air) at the interface, $\Delta n = n_h - n_g$, n_h is the host fluid viscosity, n_g is the invading guest fluid (e.g., air) viscosity, b is the gap between plates, σ is the interfacial surface tension, and λ is the finger width of the instability.[25] Simply, an invading fluid bubble will bifurcate and form branches if the left-hand term is larger than the right-hand term – e.g., if the invading guest fluid is injected fast enough to overcome surface tension.

3. Materials and Methods

We fabricated Hele-Shaw cells, comprising two rigid PMMA plates (30x30x0.6 cm^3). Plates were sealed at the seams using a 1-mm-thick double-sided elastomer adhesive (3M), creating a 1-mm-thick planar space for fluid flow. We designed Hele-Shaw cells with both a central and boundary inlet. For the former case, we milled an inlet port at the center of, and four outlet ports at the corners of, the top PMMA plate. For the latter case, we milled an inlet port along one boundary of, and two outlet ports at the opposite corner boundaries of, the top PMMA plate. We adhered luer locks to the inlet ports, and connected the luer locks to PVC tubing (1/4" I.D. x 3/8" O.D.). We fed the tubing to a NE-1010 digital syringe pump, to control flow rate and flow direction. We left all outlet ports open to the atmosphere, and filled the Hele-Shaw cell with a highly-viscous opaque molasses liquid (Fig. 1a)

To generate reversible air bubbles, we introduced air into the molasses layer confined within the Hele-Shaw cell at a controlled speed (25 mL/min) (Fig. 1b). The air first compressed, before rapidly self-assembling within the cell – at which point volume was estimated to be constant, and therefore pressure was assumed to be constant. As air bubbles displaced the molasses layer, light transmission increased through the cell. Optical transmission spectra, through both the visible and near-infrared regions, was measured with a Lambda 1050 Spectrometer (three-detector module). Time-dependent visible light intensity was measured behind the cell with an Extech HD450 Light Meter Datalogger. And time-dependent temperature was measured behind the cell with a k-type thermocouple. Bubbles were reversibly collapsed by reversing the direction of flow on the syringe pump.

By assuming Darcy Flow within this constant field (i.e., instantaneous flow rate is proportional to the pressure gradient, $q \propto \nabla P$), we were able to assume mathematical analogy to an electromotive model, where field strength is proportional to the gradient of electrostatic potential, $E \propto \nabla I$. Static, steady-state, potential flow for various flow-field configurations (i.e., isotropic and anisotropic) was accordingly approximated by calculating an electric potential field

(MATLAB, code adapted from [26]), where each inlet was prescribed a charge of +1 and each outlet a charge of -1.

4. Results

4.1. Reversible Bubble Injection

We injected an air bubble into an opaque host phase (molasses) confined within a Hele-Shaw cell (Fig. 1c). Due to the high Δn between air and molasses, the interface became unstable, and the bubble bifurcated and branched as it grew. We subsequently collapsed the bubble by switching the direction of air flow to create negative pressure (Fig. 1d). This action also switched the direction of instability – the collapsing interface became stable as Δn turned negative – demonstrating stable reversibility over bubble growth. We repeated this emergence-collapse cycle, showing good consistency and repeatability (n > 50 cycles).

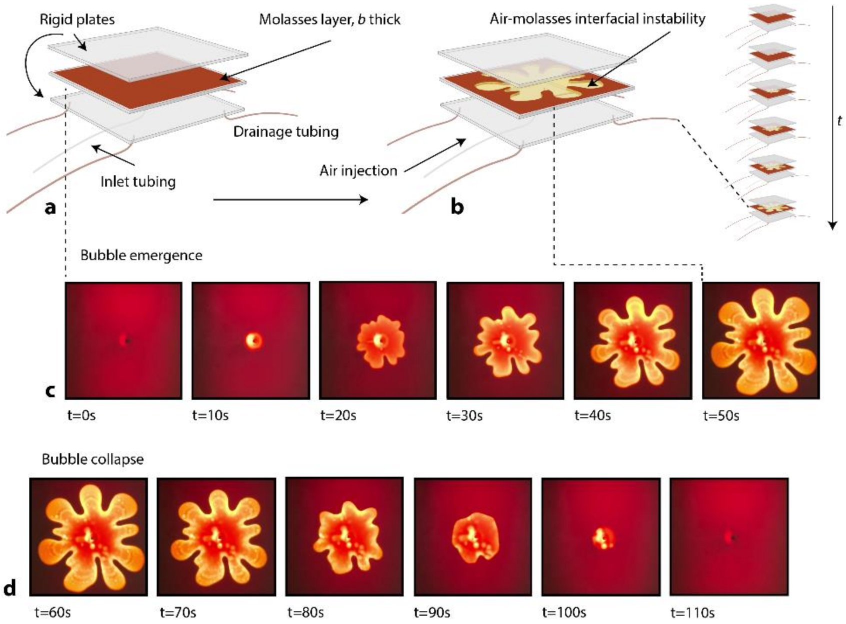

Figure 1. (a) Hele-Shaw cell filled with viscous molasses. (b) Hele-Shaw cell with radial bubble following pressurized air injection over time. (c) Images of radial bubble emergence and (d) collapse sequence over time within Hele-Shaw cell.

4.2. Tuning Bubble Morphology with Injection Rate

We injected air bubbles into an opaque molasses phase confined within a Hele-Shaw cell at different constant flow rates, ranging from 0.05-30.00 mL/min (Fig. 2a). As the flow rate increased, the width of the branches decreased, as $3V\Delta n$ grew,[19] as can be verified in the well-established derivation of equation (1) into equation (2).[19] By indirectly tuning V through control over injection flow rate of air, we can control bubble morphology within the cell.

$$(2) \qquad \lambda = \pi b \sqrt{\frac{\sigma}{V\Delta n}}$$

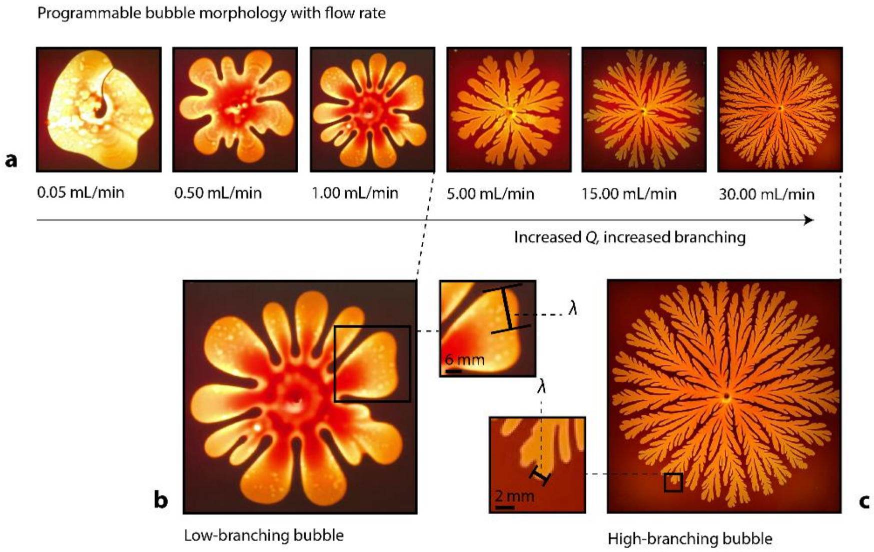

Figure 2. Programmable bubble morphology with injection flow rate. (a) Different bubble morphologies following injection, where each air bubble was injected at a different constant rate. (b-c) Comparison of relative branch width between two bubbles injected at different rates (1 mL/min versus 30 mL/min).

4.3. Tuning Bubble Morphology with Flow Field

Beyond this localized morphological control, we demonstrated control over global pattern morphology through the deliberate placement of inlet and outlet ports within a Hele-Shaw cell. The relative position of inlet and outlet ports, and the relative geometry of the confined cell, determines the static potential flow for the emerging bubble. In Fig. 3, we demonstrate relative morphology between a bubble emerging from a central injection port within a radially-isotropic flow field (Fig. 3a-b) and a bubble emerging from a boundary injection port within a directionally-biased anisotropic flow field (Fig. 3c-d). While the bubble expands radially in the former case, the bubble expands unidirectionally in the latter case. We speculate that there might be functional benefits to each of these design scenarios – most obviously, a boundary inlet enables better concealment of injection tubing over a central inlet.

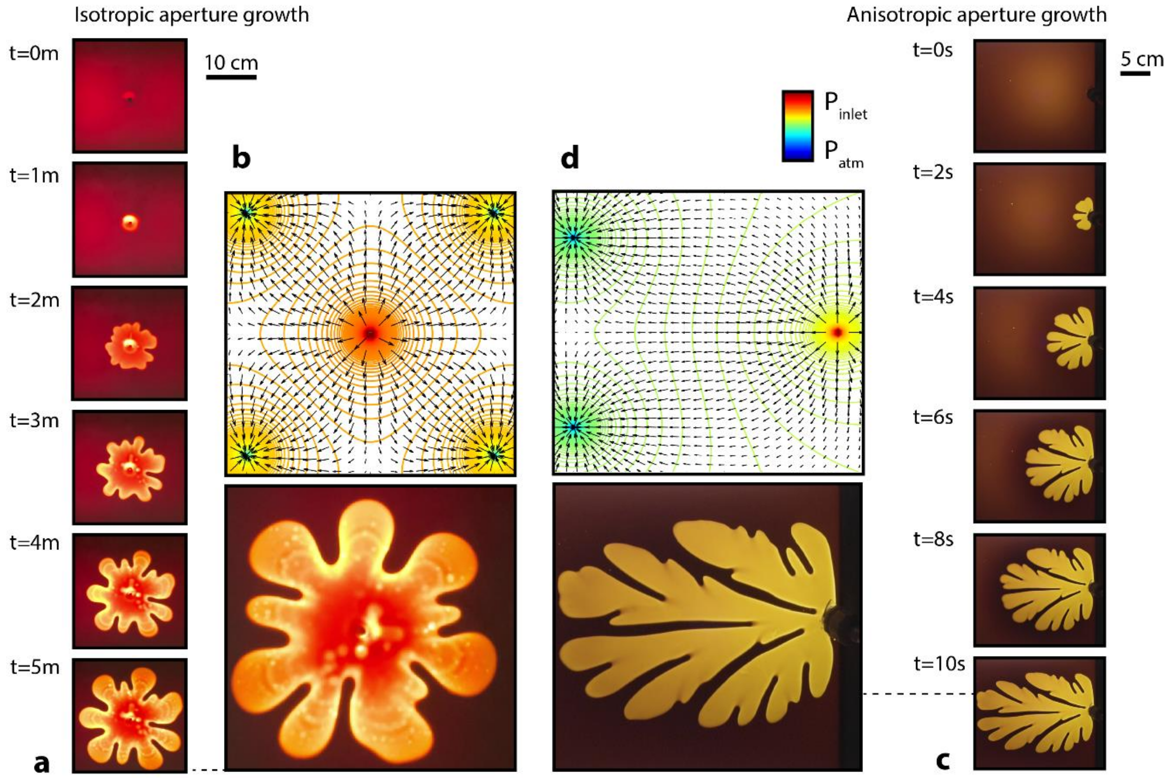

Figure 3. The effect of isotropic versus anisotropic flow field on bubble morphology. (a-b) Radially-isotropic potential flow from central inlet to equidistant boundary outlets causes radial bubble formation. (c-d) Directionally-anisotropic potential flow from boundary inlet to boundary outlets causes anisotropic, directionally-biased bubble formation.

4.4. Adaptive and Reversible Modulation of Visible Light Transmission

We injected and subsequently collapsed an air bubble within our Hele-Shaw cell. Air bubbles displaced a significant volume of the molasses layer, greatly decreasing the cross-sectional path length of molasses through which light was required to travel. We characterized the local change in visible light transmission through the cell, as a function of wavelength, for a fluidic region with and without an air bubble. For cross-sectional regions within the Hele-Shaw cell occupied by an air bubble, the average transmissivity across the visible region of the electromagnetic spectrum was measured using a spectrophotometer to be roughly 35.3% (Fig. 4b). Alternatively, for cross-sectional regions within the Hele-Shaw cell unoccupied by an air bubble (i.e., occupied completely by molasses), the average transmissivity across the visible region of the electromagnetic spectrum was measured using a spectrophotometer to be roughly 4.3% (Fig. 4b).

We then characterized the global change in visible light transmission through the entire cell, as a function of cell size across its emergence and collapse (Fig. 5a). We developed a simple 'shoebox' model (30 x 30 x 30 cm^3) to control for, and within which to measure, interior light intensity. We replaced a portion of one of the six exterior facades of the model with our fluidic cell, and illuminated the model room from the exterior using a LED light bulb (providing 300 lux into the space with the panel removed) (Fig. 5b). We measured interior light intensity from the back of this room, registering a baseline value of 15 lux prior to bubble injection (Fig. 5c), corresponding to a baseline transmissivity value of 4.5% (15/300 lux) within the visible spectrum. We injected air at a constant rate of 25 mL/min and measured both interior light intensity (Fig. 5c) and air bubble area fraction (Fig. 5d) over time. By dividing measured interior light intensity by measured incident light intensity (300 lux), we were able to characterize transmissivity through the entire cell over time (Fig. 5e) – an important property for assessing the optical performance of adaptive glazing. We report good agreeance between measured transmissivity (data points in Fig. 5e) and a theoretical prediction of transmissivity (dotted black line in Fig. 5e), calculated by taking the light transmission of the air bubble and molasses layer averaged across all visible wavelengths (350-750 nm, measured using spectrophotometry as 35.3% and 4.3%, respectively), weighted by their measured area fractions across injection. In simpler terms, this prediction entailed multiplying the measured area fraction of the air bubble by the transmissivity of the air bubble (0.353) and the measured area fraction of the molasses by the transmissivity of the molasses (0.043), and summing these products. As predicted, light transmission and transmissivity both increased as the size/area fraction of the bubble increased, and we showed that light intensity and transmissivity moved approximately linearly with bubble area fraction (Fig. 5f-g), to a maximum value of roughly 14%. In Fig. 5g, we compared measured transmissivity values (interior light intensity divided by incident light intensity) to our theoretical prediction, showing broad agreement.

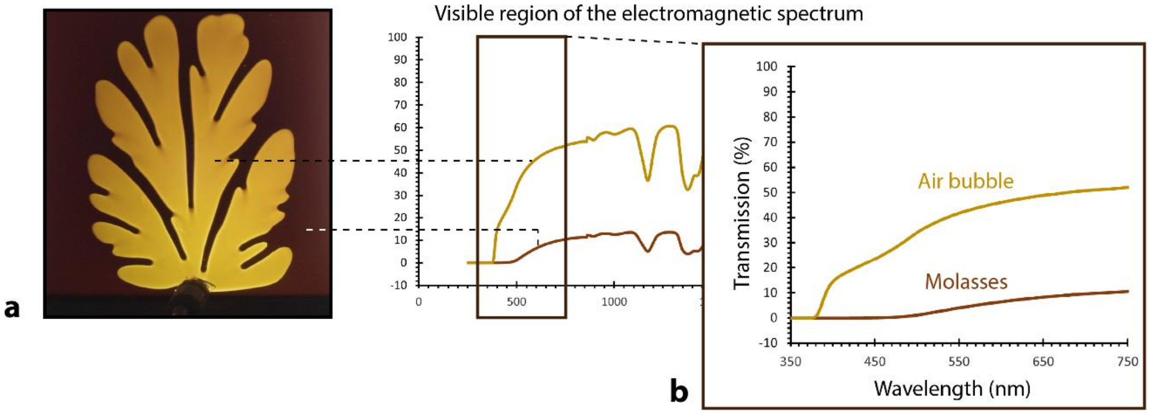

Figure 4. Local visible light transmission changes with the injection of an air bubble. (a) Air bubble fully expanded within molasses-filled Hele-Shaw cell. (b) Light transmission within the

visible region of the electromagnetic spectrum for both the molasses-filled Hele-Shaw layer with (air bubble) and without (molasses) air displacement. Average transmissivities for air bubble and molasses Hele-Shaw cell regions across the visible portion of the electromagnetic spectrum (350-750 nm) are 35.3% and 4.5%, respectively.

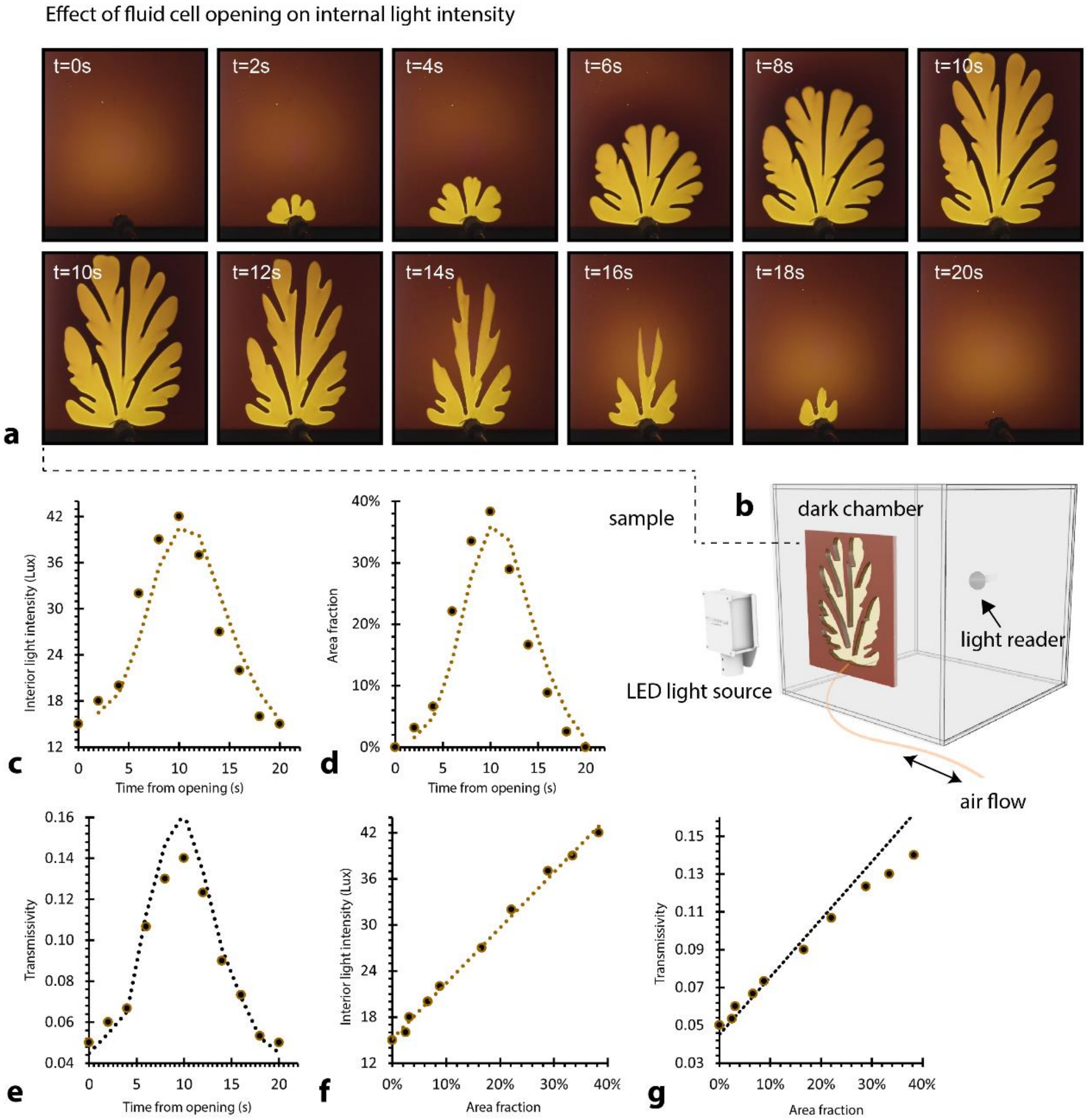

Figure 5. Modulation of visible light transmission in a Hele-Shaw cell (a) Reversible injection and collapse of air bubble within Hele-Shaw cell. (b) Schematic illustrating experiment to measure interior light intensity. (c) Change in interior light intensity over injection time. Dotted brown line represents moving average. (d) Change in bubble area fraction over injection time.

Dotted brown line represents moving average. (e) Change in cell transmissivity over time. Dotted black line represents theoretical transmissivity, calculated as the average visible transmission for air bubble and molasses fractional area components. (f-g) Interior light intensity and cell transmissivity move approximately linearly with bubble area fraction. Dotted brown line in (f) represents best fit linear trendline. Dotted black line in (g) represents theoretical transmissivity, calculated as described in (e). For simplicity, experiment illustrated in (b) conducted in the horizontal plane (setup rotated 90°).

4.5. Adaptive and Reversible Modulation of Near-Infrared Light Transmission, Solar Heat Gain, and Heat Flow

Beyond describing changes to visible light transmission, we characterized the local change in near-infrared light transmission through the cell, as a function of wavelength, for a temporary air bubble injection (Fig. 6). Similar to the effect demonstrated in the visible region of the electromagnetic spectrum, air injection caused an increase in near-infrared light transmission (Fig. 6b). Both this increase in near-infrared light transmission, and the previously demonstrated increase in visible light transmission, cause an increase in radiative heat flow across the Hele-Shaw cell. This change in radiative heat flow can be captured using a solar heat gain coefficient (SHGC),

$$(3) \qquad SHGC = T_{sol} + \frac{q_{in(I_s=0)} - q_{in}}{I_s}$$

Where T_{sol} is the total solar transmittance of the glazing system, $q_{in(I_s=0)}$ is the heat flux into the indoor environment without incident solar radiation, q_{in} is the heat flux into the indoor environment with incident solar radiation, and I_s is incident solar radiation. Here, T_{sol} of a material can be computed as the sum of the solar irradiance on earth (Fig. 6c) at each wavelength multiplied by the material transmissivity at each wavelength, all divided by the total solar irradiance on earth. If we presume that our Hele-Shaw cell is located on the exterior of a well-insulated window unit, we can assume solar heat gain through absorption and reemission, the second term of Equation (3), to be negligible. Accordingly, Equation 3 can be simplified such that the SHGC of a material is equal to the total solar transmittance of that material.

Using the transmissivity data in Fig. 6b, we calculated the SHGC of our Hele-Shaw cell cross-section with both an air bubble present and without, finding a SHGC of 43% and 7%, respectively. These SHGCs represent functional bounds to the performance of our system, where our cell prior to an air injection can transmit 7% of solar radiation and a cell after a maximum air injection covering 100% of the total area can transmit 43% of solar radiation. Using data on the area fraction of an air bubble over a complete injection and retraction sequence (demonstrated in Fig. 5a), we calculated the effective SHGC of the cell at each time step by multiplying the air bubble area fraction by 0.43 and the molasses area fraction by 0.07, and summing these components

(Fig. 6d). Effective SHGC accordingly moved linearly with air bubble area fraction, as the effective SHGC of the cell increased from 7% to 21% for a change in area fraction from 0-39% (Fig. 6e).

To experimentally validate this result, we developed a similar ‘shoebox’ model as described in the proceeding section (30 x 30 x 30 cm^3), but removed four of the six walls to assess the effect of radiative heat transfer in a well-ventilated space (i.e., isolating radiative heat transfer) (Fig. 7b). To provide radiative energy, we illuminated the cell with a 50-W incandescent light bulb (Fig. 7b), and allowed a thermocouple measuring the temperature of a PMMA sheet within the space to reach a thermal equilibrium (after 30 minutes) of 30 ℃ prior to bubble injection (Fig. 7c, t=1 min). We then injected air at a constant rate of 25 mL/min for 10 seconds, injecting approximately 4 mL. As predicted, the temperature of the interior PMMA sheet began to increase after the air bubble was injected, reaching a new thermal equilibrium of 37 ℃ after nine minutes (Fig. 7c). Six minutes later, we collapsed the bubble, and observed a reversible radiative thermal effect, where the temperature of the interior sheet decreased back to below 30 ℃ (Fig. 7c, t=27 min).

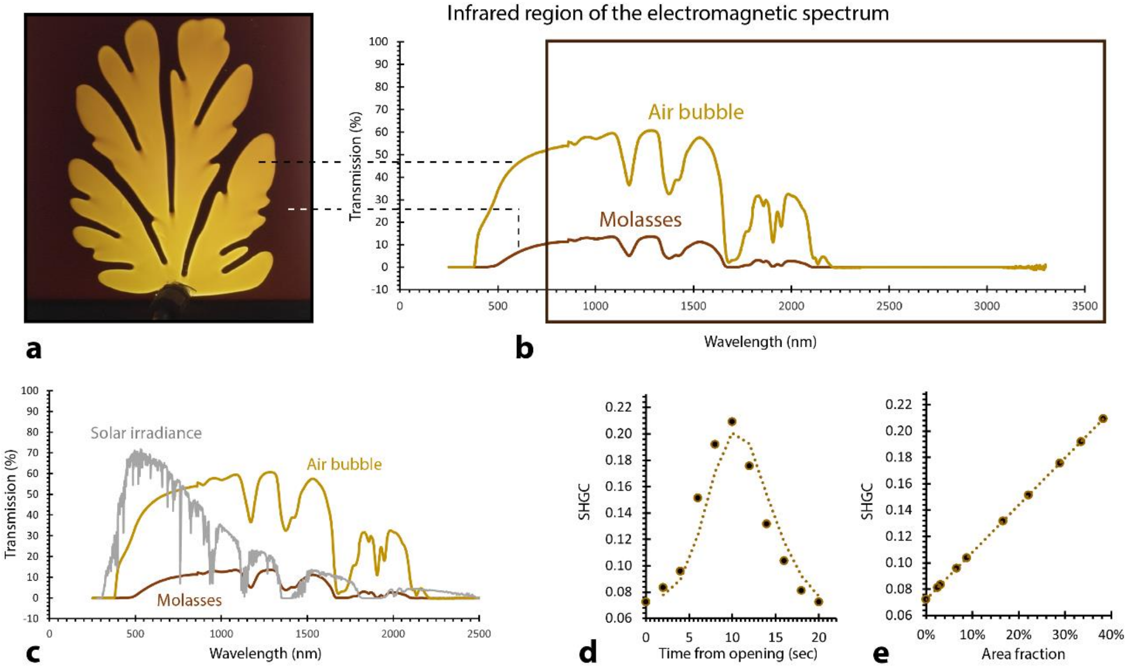

Figure 6. Local near-infrared light transmission and solar heat gain changes with the injection of an air bubble. (a) Air bubble fully expanded within molasses-filled Hele-Shaw cell. (b) Light transmission within the near-infrared region of the electromagnetic spectrum for both the molasses-filled Hele-Shaw layer with (air bubble) and without (molasses) air displacement. (c) Light transmission data from (b) overlaid atop solar radiation spectrum on earth, where radiation values are represented in units along the y-axis of 50 W/m^2/nm (data from National Renewable Energy Laboratory). Solar heat gain coefficient (SHGC) for air bubble and molasses

region is 43% and 7%, respectively. (D) Effective solar heat gain coefficient of Hele-Shaw cell over time (same experiment as depicted in Fig. 5a), where effective SHGC is measured as the area-normalized SHGC of the air bubble and molasses regions of the cell. (E) SHGC therefore moves linearly with air bubble area fraction.

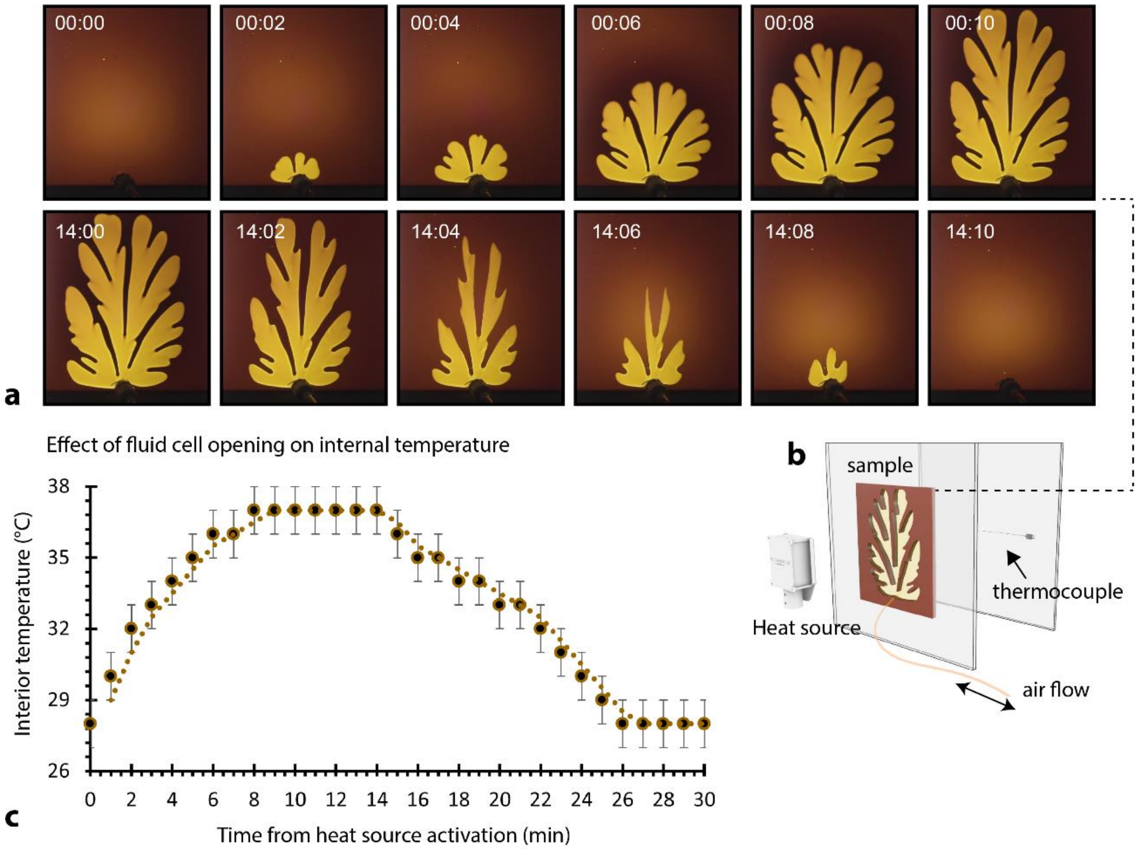

Figure 7. Modulation of near-infrared light transmission in a Hele-Shaw cell (a) Reversible injection and collapse of air bubble within Hele-Shaw cell. (b) Schematic illustrating experiment to measure interior temperature. (c) Change in interior temperature over time with air bubble injection and collapse. For simplicity, experiment illustrated in (b) conducted in the horizontal plane (setup rotated 90°).

4.6. Motion-induced Digital Bubble Response

To demonstrate the potential of this material system within a responsive building facade, we developed a digital feedback system to couple the electrical input of an ultrasonic distance sensor (Parallax 28015) to the electric output of a peristaltic pump (INTLLAB 12V). We programmed two distance thresholds, such that a hand wave within 10 cm of the cell-integrated sensor would drive the injection of an air bubble, and a hand wave between 10.1 cm and 30 cm from the cell would drive the collapse of that air bubble. We demonstrated this ultrasonic-fluidic feedback over several cycles – one of which is demonstrated over a 12 second time-scale in Fig. 8.

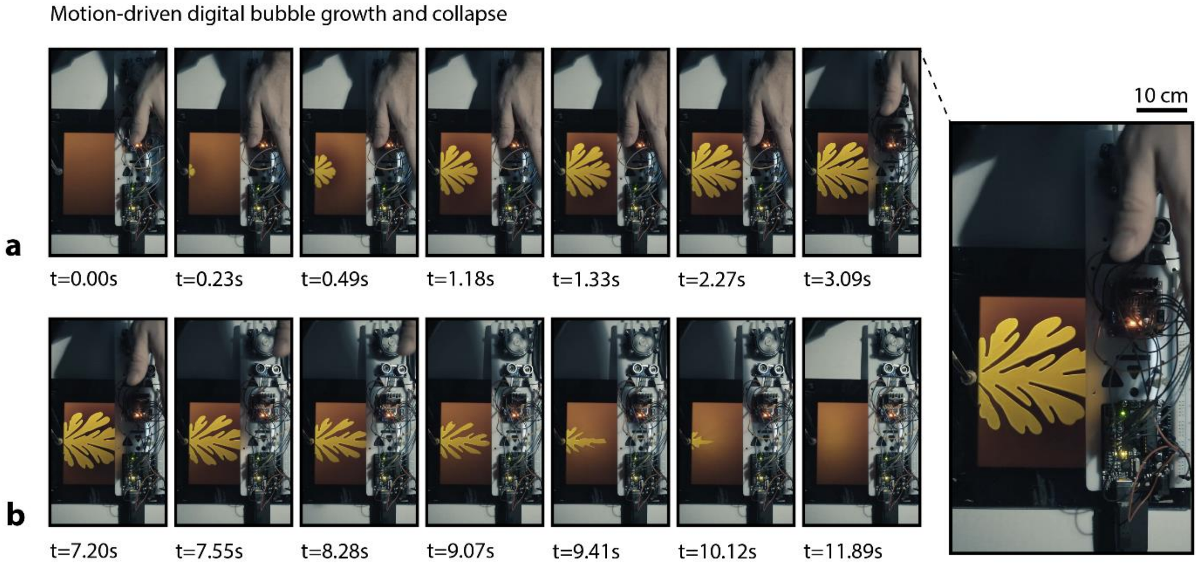

Figure 8. Tunable ultrasonic detection can drive a proportional fluidic response. (a) Injection of air bubble proportional to the amount of time a hand is detected within the forward-growing distance threshold (0.1-10 cm). (b) Collapsing of air bubble proportional to the amount of time a hand is detected within the backward-growing distance threshold (10.1-30 cm).

4.7. Modelled Building Energy Consumption

4.7.1. Simulation Setup and Control Algorithm

To demonstrate the energy performance of our active fluid layer, we used a building energy modelling tool (EnergyPlus) to estimate the annual energy required for heating, cooling, and lighting a conventional office space locating in Toronto, Canada. In particular, we compared energy costs for conditioning the space when clad along its south face with (i) our switchable Hele-Shaw cell, (ii) a state-of-the-art electrochromic (EC) window, (iii) a dynamic roller shade (RS) interior to a double-glazed window, and (iv) a static low-emissivity control double-glazed window. The one-zone reference office, illustrated in Fig. 9a and described in detail in [27], is 3.6 m wide (E-W direction) and 8.2 m deep (N-S direction), with a south-facing window (window-to-wall ratio of 88%). For consistency, we simulated the operation of each of these three dynamic systems (i-iii) using a standard control algorithm, designed as a naïve energy minimizer, restricted to maintain a set illuminance of 300 lux across 50% of the model floor area during each occupied hour. Additionally, the algorithm restricted the over-lit area (defined as exceeding 3000 lux) to less than 10% of the model floor area.

We modelled our Hele-Shaw cell to switch between seven possible states, derived from the effective transmission spectra for a Hele-Shaw cell with air bubble area fractions between 0%

and 60% (at 10% steps) (transmission spectra shown in Fig. 9b, left). We note that an air bubble area fraction of 60% represents an upper functional limit that we observed in our physical experiments in square-shaped Hele-Shaw cells. We modelled the EC window to switch between four standard states (transmission spectra taken from a real market product, and shown in Fig. 9b, center). And, finally, we modelled the RS to switch between its two standard states (up and down), where the 'up' state corresponded to the transmission spectra of a double-pane control window by itself (Fig. 9b, right). To account for building integration, the EC window and Hele-Shaw cell were modelled on the exterior, and the RS was modelled on the interior, of a standard double-pane window. This standard control window had a visible transmittance value of 81%, a SHGC of 71%, and a conductive heat transfer coefficient (U-value) of 1.81 W/m^{2}K. Our seven Hele-Shaw cell states (Fig. 9b, left), when combined with the standard control window, had visible transmittance values of 22, 19, 16, 13, 9, 7, and 4%, and SHGC values of 23, 20, 17, 14, 11, 9, and 6%, respectively.

We assumed a standard hourly occupancy schedule for the office,[28] with a baseline occupancy density of 0.053821313 m^2/person. For every hour in which the space was occupied, each available control state (defined in Fig. 9b for each dynamic system) was tested to satisfy the required illuminance and overlighting constraints. For each material state meeting these constraints, solar heat gain and electric lighting utilization were calculated. Once the acceptable daylight-driven requirements were met, a heat balance was calculated at each hour based on thermal model outputs for internal heating loads (occupants, lights, equipment) and external heating loads (ventilation, solar heat gains, conduction). Of all calculated material states, the state that minimized total energy (combined heating, cooling, and lighting) was selected. Because the underlying thermal models are transient in nature (i.e., each timestep influences the next), the control algorithm was iterated many times until annual energy results stabilized. This allowed a near-optimal control system to be achieved.

Within the reference office, all non-exterior walls, floors, and ceilings were defined to be adiabatic. All opaque walls were modelled with a U-value of 0.472 W/m^{2}K, and all other indoor materials were modelled with conventional IES LM-83 material properties. We used a fresh air supply of 0.0125 m^3/s/person, and assumed that 70% of sensible heat and 65% of latent heat was recovered by the heat-recovery system. Each person generated heat at a rate of 125 W, and all equipment was modelled with a peak power density of 5 W/m^2, with an hourly schedule as defined by the National Energy Code of Canada for Buildings.[28] While the building was occupied, we defined temperature setpoints at 21 and 24 ℃, and at 15.6 and 26.7 ℃ otherwise. We used an electric lighting power across the space of 99 W, (3.4 W/m^2), where lights were activated daily between 7:00-19:00, and were dimmed to reduce thermal gains and simultaneously meet the target illuminance.

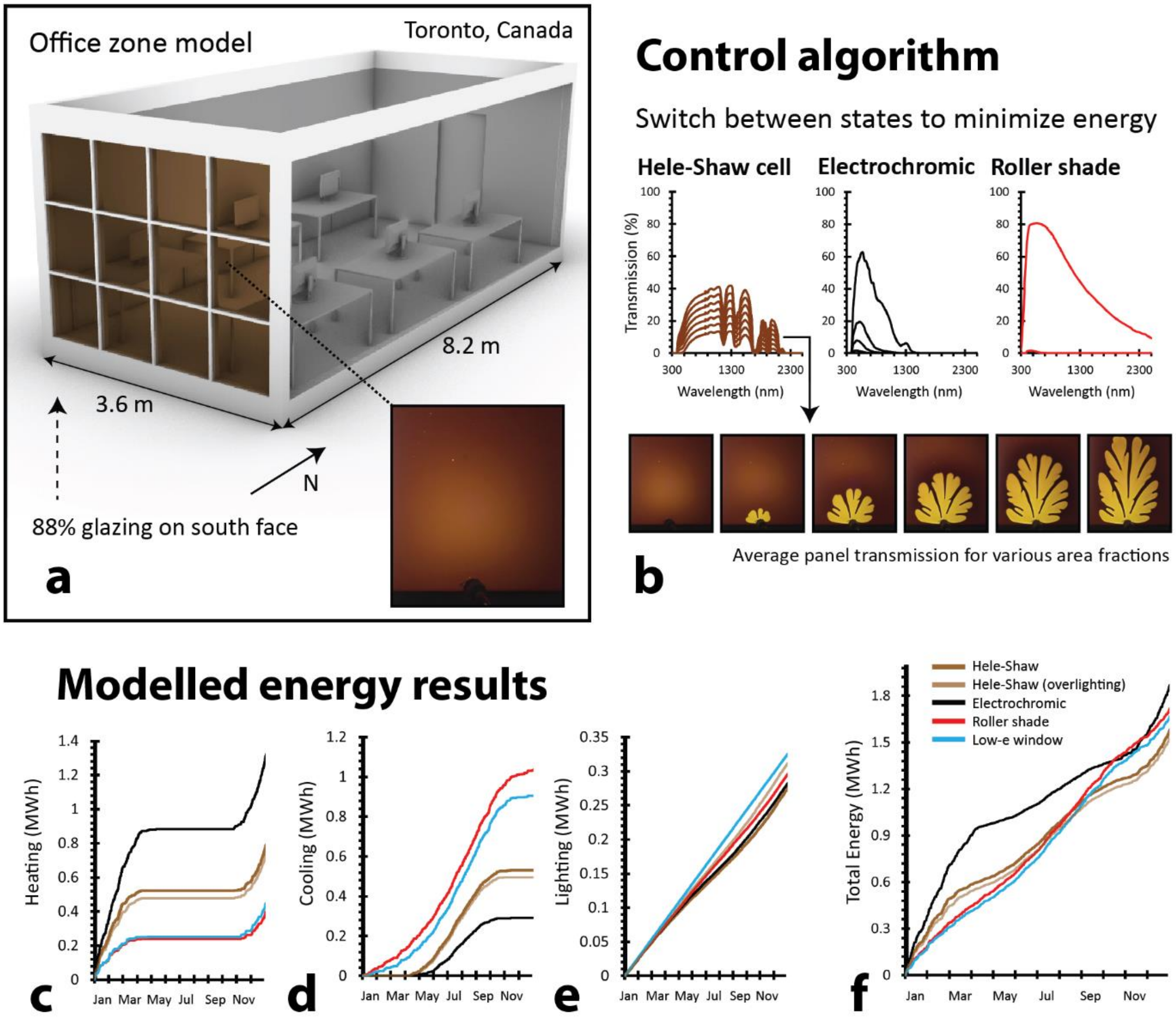

Figure 9. Comparative energy performance of active Hele-Shaw cell. (a) Reference office model for energy simulations. Note: roof and walls are translucent only for illustrative clarity, and were modelled as opaque elements in simulation. (b) Available control states for dynamic switching of Hele-Shaw cell, EC window, and RS. (c-f) Simulated cumulative annual heating, cooling, and electric lighting energy usage for office space cladded in Hele-Shaw cell (both with limited and unlimited spatial overlighting), EC window, RS, and control window. (g) Total simulated cumulative annual energy data for Hele-Shawl cell, EC window, RS, and control window, demonstrating superior energy performance by Hele-Shaw cell.

4.7.2. Simulation Results

In simulation, we found that the dynamic operation of our Hele-Shaw cell could reduce total annual operation energy usage in our office space by 16%, 7%, and 4% over EC, RS, and static glazing systems, respectively (Fig. 9f). The roller shade and static control window followed similar temporal consumption trends (Fig. 9f), requiring, in comparative terms, much more energy to achieve cooling than heating (Fig. 9c-d). Conversely, the EC window and Hele-Shaw cell followed similar temporal consumption trends (Fig. 9f), requiring, in comparative terms, much more energy to achieve heating than cooling (Fig. 9c-d). Despite this consumption trend similarity, our Hele-Shaw cell required much less energy than did the EC window to heat the indoor space (Fig. 9c), resulting in reduced energy consumption compared with the EC system. This performance difference was likely achieved by the fact that our Hele-Shaw system can admit much more near-infrared light for each unit of admitted visible light (compare spectral distributions in Fig. 9b), enabling higher solar heat gains within a given limit of overlighting. We found that electric lighting consumption played a smaller role in total energy consumption, and that all systems performed comparatively across the year (Fig. 9e).

We also compared relative energy performance by adjusting the control algorithm to allow for spatial overlighting (>3000 lux) above 10% within the space. With this overlighting constraint removed, we found that the dynamic operation of our Hele-Shaw cell could now reduce total operational energy usage in our office space by 36%, 10%, and 7% over EC, RS, and static glazing systems, respectively (Fig. 9f). While this change in operational control likely increases glare and optical discomfort, it reduces electric lighting costs, unwanted lighting-induced cooling costs, and enables more solar heat gain when required to reduce mechanical heating costs.

4.7.3. Operational Energy Cost Calculation

Finally, to assess the feasibility of building integration, we estimated the energy required to optimally operate our fluidic Hele-Shaw cell across the year. We calculated the annual operational energy as the energy required for a typical peristaltic pump to inject or retract an air bubble within a 0.25 m^2 panel in our experiments (5 W * 4 s), multiplied by the number of times an injection or retraction occurred in our annual energy simulation (1630), multiplied by the number of 0.25 m^2 panels needed to cover the south-face glazing (9.5 m^2) of our one-zone simulation space (38). We obtained an estimated energy operational energy cost of 0.344 kWh, or about 0.12% of the energy that our dynamic Hele-Shaw system could save over an EC window in our simulation (303.5 kWh). This result importantly suggests that our Hele-Shaw cell might have only a negligible operational energy cost, validating building integration feasibility.

5. Discussion

We developed a methodology to translate well-established nonlinear fluid dynamics to responsive building facades in architecture. We demonstrated shape- and size-tunable bubble injections to modulate both visible light transmission and near-infrared heat gain within a mockbuilding interface, and achieved reversibility over multiple cycles. We then simulated the energetic performance of our system within a prototypical office model, and found that the dynamic operation of our Hele-Shaw system (switching between air injection states that cover 0-60% of the model's south-facing facade) could reduce annual energy consumption by up to 36% over a state-of-the-art electrochromic window. Our experimental and modelled results suggest building integration feasibility, with the potential for substantial improvements to architectural energy efficiency.

5.1. Future Considerations

Because the interface between air and the opaque host phase (in this case, molasses) is highly unstable, the branched pattern morphology of the injected bubble represents only a meta-stable state, where the resistance to flow of the molasses phase enables longer-term (minutes-hours) pattern stability. In thermodynamic terms, decay of the branching state is inevitable over time, but the time-scale of branch-decay for these specific fluids must be better understood in order to assess the limitations in long-term patterning and light transmission within a Hele-Shaw cell.

Similarly, while buoyant forces had a negligible impact on bubble morphology for injections within vertically-oriented cells (t=40 min), the decay of bubble morphology may be amplified by gravitationally-induced forces arising from the difference in density between host-molasses and guest-air phases. Future work might explore multiphase systems with fluids (liquids in particular) of the same density.

In an architectural context, the system described here can only partially control visible light transmission (visible light transmissivity ranges between 4-35%, with low specular transmission). This property is unattractive in modern building facades, where views to the outdoors are universally expected, achieved through high specular transmissivity in the visible region of the electromagnetic spectrum. From a design point of view, we speculate that, by decreasing the flow rate of the injected air bubble and increasing the hydrophobicity of the inner Hele-Shaw cell surface, we might achieve increased displacement of the host phase (i.e., increased surface wetting by the air phase). This effect, explained by Bretheten,[29] would result in a decreased molasses path length through which light would be required to travel, increasing the maximum light transmissivity, and specular light transmissivity, through the cell.

Alternatively, rather than as a replacement for traditional glazing, we envision that the demonstrated fluidic control might be desirable along both traditionally-opaque vertical (e.g., walls) and horizontal (e.g., rooves) elements within buildings – where visual clarity is not a necessity, but tunable control over visible and near-infrared light transmission remains critical for energy efficiency. In broad terms, we imagine that buildings might be entirely encapsulated by fluidic layers, enabling an improved spatial resolution of optical properties, rather than the stubborn paradigm of fixed transmission elements (windows) and fixed insulating elements (walls).

Importantly, we also note that the mechanism introduced here is generalizable. Air can be injected within a range of host liquid chemistries, where the viscosity and transmissivity of the host liquid can be selected to control the lifetime and rate of descent of an air bubble and the range of optical transparency of the Hele-Shaw panel.

Finally, we suspect that the scope of this work can far exceed energy-efficient building design. Because the morphology of air bubbles can be tuned using digital control, we imagine that large, independently-addressable, multicell arrays might be easily developed to provide visual feedback through dynamic patterning. Accordingly, such a system could be applied across both soft and hard material interfaces, with possible applications for active color change and camouflage in wearables, sensors, communication technologies, and vehicles.

6. Conclusions

This paper describes a multifluidic interface for achieving reversible injections of self-organizing air bubbles. Through digitally-controlled fluidic actuation, we demonstrate tunability over both measured visible and near-infrared light transmission, with architectural implications for both interior daylighting and solar heat gain. This work represents an early exploration into multifluidic chromogenic building facades, and we speculate that its future incarnations might enable more advanced material responses in architecture, and elsewhere.

Data Availability Statement

No datasets were generated or analyzed during the current study. All data can be made available by the authors upon request.

Competing Interests Statement

The authors declare no competing interests.

Acknowledgements

We thank David Correa for his time reviewing the manuscript.

Funding

Canadian Foundation for Innovation (CFI) #31799 (BDH)

Percy Edward Hart Professorship, University of Toronto (BDH)

RK was supported by a Canada Graduate Scholarship, a C.W. Bowman Graduate Scholarship, and a Bert Wasmund Graduate Fellowship.

Author contributions

Conceptualization: RK, KN

Methodology: RK, KN, CK, NH

Physical experimentation: RK, KN

Simulation design and implementation: JAJ

Visualization: RK

Electronic system design: KN

Funding acquisition: BDH

Writing – original draft: RK

Writing – review and editing: RK, CK, JAJ, NH, BDH

References

1. Loonen RCGM, Trčka M, Cóstola D, et al. Climate adaptive building shells: State-of-the-art and future challenges. *Renewable and Sustainable Energy Reviews* 2013; 25: 483-493. DOI: https://doi.org/10.1016/j.rser.2013.04.016.
2. Craig S and Grinham J. Breathing walls: The design of porous materials for heat exchange and decentralized ventilation. *Energy and Buildings* 2017; 149: 246-259. DOI: https://doi.org/10.1016/j.enbuild.2017.05.036.
3. Wang Y, Runnerstrom EL and Milliron DJ. Switchable Materials for Smart Windows. *Annu Rev Chem Biomol Eng* 2016; 7: 283-304. 2016/03/30. DOI: 10.1146/annurev-chembioeng-080615-034647.
4. Khandelwal H, Schenning APHJ and Debije MG. Infrared Regulating Smart Window Based on Organic Materials. *Advanced Energy Materials* 2017; 7: 1602209. DOI: 10.1002/aenm.201602209.
5. Hee WJ, Alghoul MA, Bakhtyar B, et al. The role of window glazing on daylighting and energy saving in buildings. *Renewable and Sustainable Energy Reviews* 2015; 42: 323-343. DOI: https://doi.org/10.1016/j.rser.2014.09.020.
6. Konstantoglou M and Tsangrassoulis A. Dynamic operation of daylighting and shading systems: A literature review. *Renewable and Sustainable Energy Reviews* 2016; 60: 268-283. DOI: https://doi.org/10.1016/j.rser.2015.12.246.
7. Drozdowski Z and Gupta S. Adaptive Fritting as Case Exploration for Adaptivity in Architecture. In: *Proceedings of the 29th Annual Conference of the Association for Computer Aided Design in Architecture* Chicago, Illinois, October 22-25 2009, pp.105-109.
8. Lienhard J, Schleicher S, Poppinga S, et al. Flectofin: a hingeless flapping mechanism inspired by nature. *Bioinspiration & Biomimetics* 2011; 6: 045001. DOI: 10.1088/1748-3182/6/4/045001.
9. Park D, Kim P, Alvarenga J, et al. Dynamic daylight control system implementing thin cast arrays of polydimethylsiloxane-based millimeter-scale transparent louvers. *Building and Environment* 2014; 82: 87-96. DOI: https://doi.org/10.1016/j.buildenv.2014.07.016.
10. Viereck V, Ackermann J, Li Q, et al. Sun glasses for buildings based on micro mirror arrays:

Technology, control by networked sensors and scaling potential. In: *2008 5th International Conference on Networked Sensing Systems* 17-19 June 2008 2008, pp.135-139.

11. Wood DM, Correa D, Krieg OD, et al. Material computation—4D timber construction: Towards building-scale hygroscopic actuated, self-constructing timber surfaces. *International Journal of Architectural Computing* 2016; 14: 49-62. DOI: 10.1177/1478077115625522.

12. Reichert S, Menges A and Correa D. Meteorosensitive architecture: Biomimetic building skins based on materially embedded and hygroscopically enabled responsiveness. *Computer-Aided Design* 2015; 60: 50-69. DOI: https://doi.org/10.1016/j.cad.2014.02.010.

13. Poppinga S, Zollfrank C, Prucker O, et al. Toward a New Generation of Smart Biomimetic Actuators for Architecture. *Advanced Materials* 2018; 30: 1703653. https://doi.org/10.1002/adma.201703653. DOI: https://doi.org/10.1002/adma.201703653.

14. Granqvist CG. Chromogenic materials for transmittance control of large-area windows. *Critical Reviews in Solid State and Materials Sciences* 1990; 16: 291-308. DOI: 10.1080/10408439008242184.

15. Lampert CM. Chromogenic smart materials. *Materials Today* 2004; 7: 28-35. DOI: https://doi.org/10.1016/S1369-7021(04)00123-3.

16. Granqvist CG, Lansåker PC, Mlyuka NR, et al. Progress in chromogenics: New results for electrochromic and thermochromic materials and devices. *Solar Energy Materials and Solar Cells* 2009; 93: 2032-2039. DOI: https://doi.org/10.1016/j.solmat.2009.02.026.

17. Cupelli D, Nicoletta FP, Manfredi S, et al. Electrically switchable chromogenic materials for external glazing. *Solar Energy Materials and Solar Cells* 2009; 93: 329-333. DOI: https://doi.org/10.1016/j.solmat.2008.11.010.

18. Lee ES and DiBartolomeo DL. Application issues for large-area electrochromic windows in commercial buildings. *Solar Energy Materials and Solar Cells* 2002; 71: 465-491. DOI: https://doi.org/10.1016/S0927-0248(01)00101-5.

19. Saffman PG and Sir Geoffrey Taylor FRS. The penetration of a fluid into a porous medium or Hele-Shaw cell containing a more viscous liquid. In: Pelcé P (ed) *Dynamics of Curved Fronts*. San Diego: Academic Press, 1958, pp.155-174.

20. Hill S and P FI. Channeling in packed columns. *Chemical Engineering Science* 1952; 1: 247-253. DOI: https://doi.org/10.1016/0009-2509(52)87017-4.

21. Kessler DA, Koplik J and Levine H. Pattern selection in fingered growth phenomena. *Advances in Physics* 1988; 37: 255. DOI: 10.1080/00018738800101379.

22. Bischofberger I, Ramachandran R and Nagel SR. Fingering versus stability in the limit of zero interfacial tension. *Nature Communications* 2014; 5: 5265. DOI: 10.1038/ncomms6265.

23. Bischofberger I and Nagel SR. Fluid instabilities that mimic animal growth. *Physics Today* 2016; 69: 70-71.

24. Bischofberger I, Ramachandran R and Nagel SR. An island of stability in a sea of fingers: emergent global features of the viscous-flow instability. *Soft Matter* 2015; 11: 7428-7432. 10.1039/C5SM00943J. DOI: 10.1039/C5SM00943J.

25. Saffman PG and Taylor GI. The penetration of a fluid into a porous medium or Hele-Shaw cell containing a more viscous liquid. *Proceedings of the Royal Society of London Series A*

Mathematical and Physical Sciences 1958; 245: 312-329. DOI: 10.1098/rspa.1958.0085.

26. Donadio L. Electric Potential and Electric Field. https://github.com/lorenzolds/partitions/issues/2 2016.

27. Reinhart CF, Jakubiec JA and Ibarra D. Definition of a reference office for standardized evaluations of dynamic façade and lighting technologies. In.

28. National Energy Code of Canada for Buildings 2017.

29. Bretherton FP. The motion of long bubbles in tubes. *Journal of Fluid Mechanics* 1961; 10: 166-188. 2006/03/28. DOI: 10.1017/S0022112061000160.